RESEARCH PAPER

The Effect of Shock Compression on the Crystal Structure of Cryptomelane (K-OMS-2)

M. Murchland[1,3] · S. Elasamar[1,3] · G. Viner[1,3] · X. Zhou[4,6] · M. Gillis[1] · C. Almquist[5] · B. Cymes[1] · M. Bhowmick[3] · C. L. McLeod[1] · M. P. S. Krekeler[1,2]

Abstract

Cryptomelane K-OMS-2 is a manganese oxide that occurs in low temperature geologic environments and is readily synthesized in the lab. A reflux method was used to prepare cryptomelane K-OMS-2 for shock compression experiments using laser driven flyer plates. Powder X-ray diffraction data indicates that cryptomelane K-OMS-2 is shock resistant and largely retains crystallinity, with some major reflections increasing in peak sharpness with others broadening slightly. Transmission electron microscopy data indicates particle size and morphology of shocked material is also largely retained but crystals have amorphous regions near the surfaces, have deformed lattice fringes, and have streaked electron diffraction characteristics. Raman spectroscopy indicates that shock has altered the structure of cryptomelane, with the 570 cm^{-1} band-shift probably corresponding to a slight decrease in bond length and a dramatic change in band intensity for the 641 cm^{-1} may be evidence of increasing disorder, and the shift towards lower frequency could be resulted from an increased bond length. The mechanism for shock resistance for these materials is proposed to be a thixotropic rebound where nanoporosity allows for crystals to migrate and the texture then returns to the approximate original position after the shock wave has passed. This investigation opens new areas of research in shock research for mineral stability.

Keywords Shock compression · Shock resistance · Cryptomelane K-OMS-2 · Transmission electron microscopy

Introduction

Manganese oxides with tunnel structures have been materials of interest for decades because of their abundance in nature and for their wide variety of intriguing physical/

✉ M. P. S. Krekeler
krekelmp@miamioh.edu

[1] Department of Geology and Environmental Earth Science, Miami University, Oxford, OH 45056, USA

[2] Department of Mathematical and Physical Sciences, Miami University Hamilton, Hamilton, OH 45011, USA

[3] Department of Mathematical and Physical Sciences, Miami University Middletown, Middletown, OH, USA

[4] School of Chemical Sciences, University of Illinois, Urbana-Champaign, Urbana, USA

[5] Department of Chemical, Paper, and Biomedical Engineering, Miami University, Oxford, OH 45056, USA

[6] Present Address: Department of Physics & Astronomy, University of Texas at San Antonio, San Antonio, TX 78249, USA

chemical properties viable for technological applications [1, 2]. Although these manganese oxide-based minerals have been extensively investigated, detailed understanding of their phases as well as their transformation mechanisms are not well understood [1] Naturally occurring Mn-oxides are known to have small particle sizes at the time of their formation, later to be modified into larger dimensions during their many years of existence (typically of the order of geologic time scales) (e.g., [3]).

Cryptomelane K-OMS-2 is a manganese oxide that occurs in low temperature geologic environments and is readily synthesized in the lab. The idealized empirical chemical formula is $K(Mn^{4+}, Mn^{2+})_8O_{16}$ however Mn^{3+} cations are known (or are likely to occur) in some samples (e.g., [4]). The molecular weight is 734.59 g/mol. The material ideally consists of 5.32% potassium (K), 59.83% manganese (Mn), 34.85% oxygen (O) and has both monoclinic and tetragonal polymorphs. For the monoclinic version, the unit cell parameters are a = 9.79 Å, b = 2.88 Å, c = 9.94 Å and β = 90.62°. This defines a unit cell volume of 280.24 Å^3 and a calculated density is 4.35 g/cm^3. Details on the crystal structure can

be found in Post et al. [5]. In summary, the crystal structure consists of four rows of double manganese octahedra (2×2) that create a tunnel which has sites for K^+ cations which can exchange for molecular water and other cations (Fig. 1).

In addition to a wide variety of natural occurrences, cryptomelane can also be synthesized easily in the laboratory (e.g., [6–17]). The main interest in cryptomelane is focused on the catalytic abilities it shows, owing to its excellent surface chemistry [14, 18–26]. Apart from the cationic exchanges in the tunnel structures or the mobile lattice oxygen, the surface area itself plays a major role in the catalysis reactions [8]. In the past, doping with transition metals such as Fe, Co, Ni, Cu, V, Cr, and Eu has been explored (e.g., [6, 8, 11, 13–15]).

Considering the role of surface area in catalysis, an alternative to actively doping cryptomelane could be to subject the material to extreme conditions, that is, to apply a very high level of compression to the material. There are several ways of compressing a material. High pressure experiments performed under static conditions using diamond anvil cells (DAC) are effective in applying longer term moderate compression along the isotherm of the sample [27]. Dynamic compression events such as shock wave experiments described in this study can subject the material to an ultra-high-pressure pulse. Effects of shock waves on rocks and minerals are manifold, as described by previous researchers [28–33]. Shock wave compression of materials has successfully been used to probe structural changes, chemical initiation, mechanochemistry, and catalysis in the recent past [34–39]. Shock metamorphism includes grain boundary fusion, phase changes, conversion into glassy materials, development of microstructures and introduction of unusual strains [30]. In addition to rapid changes in surface chemistry, shock wave loading on inorganic materials shows exciting potential for high-pressure assisted synthesis [40–43]. The phase transformation of hollandite [40] and structural changes in zinc ferrite [41] under high pressure are of particular interest from the materials science perspective. Clearly, compression with precise diagnostics could be explored more closely to optimize catalysis in minerals such as cryptomelane, and doing so would open potential for a more rapid, environmentally friendly, solvent-free manufacturing approach for the future [10].

In this paper, we report shock wave compression experiments using laser-driven flyer plates in powdered cryptomelane. A flyer is a fast-moving tiny disc made of typically metal foil, which delivers a planar shock into the sample, thereby compressing it to an ultrahigh pressure. The amount and duration of compression depends on the speed and thickness of flyers, respectively. The shock compressed cryptomelane samples, recovered after single shot experiments, were characterized using transmission electron microscopy (TEM), powder X-ray diffraction (XRD), and confocal Raman measurements to report possible physical/structural changes in them.

Materials and Methods

Materials

A reflux method was used to prepare cryptomelane K-OMS-2. This was adapted from that of Luo et al. [20] and Almquist et al. [44]. Cryptomelane K-OMS-2 was prepared in steps. First a solution was prepared with 11 g of Mn-acetate that was dissolved in 40 ml of deionized water prior to 5 ml of glacial acetic acid being added to the solution. This solution was then brought to 90 °C under stirring in a round-bottomed flask fitted with a reflux condenser. A second solution was prepared with 6.5 g of K-permanganate dissolved in
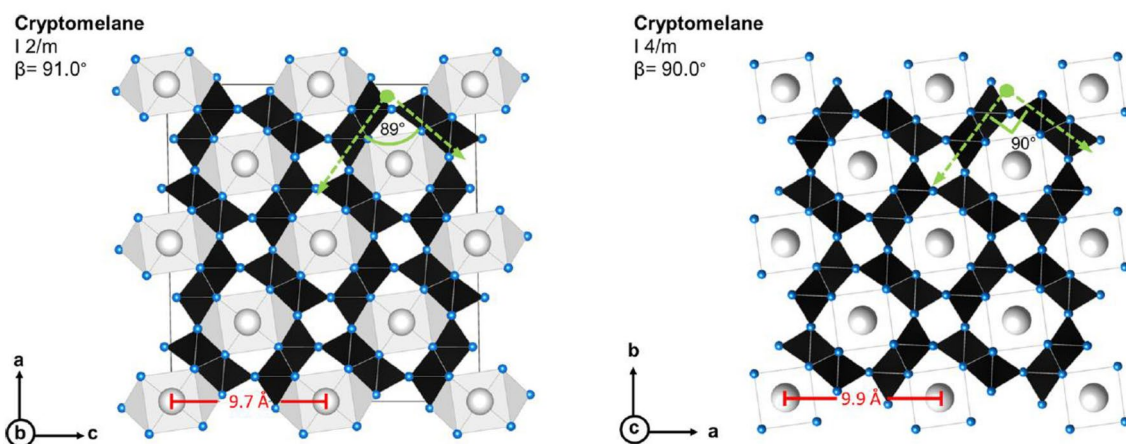

Fig. 1 Models of cryptomelane with gray spheres indicating K positions, black octathedra representing Mn-octahedra and blue spheres representing O. The left image is a monoclinic model of cryptomelane (I 2/m) and right image shows tetragonal model (I4/m)

150 ml of deionized water. This solution was slowly (drop-wise) added to the Mn acetate solution. The combined solution was then maintained at 90 °C for 24 h, with the flask suspended in a circulating water bath to ensure even-heating. The resulting precipitate was then filtered and washed several times with deionized water. The solids were then air-dried overnight at 80 °C and calcined at 450 °C for 24 h. The samples were in loose powder form as a final product of the above process. For the shock compression experiments, the loose powder was mixed with water and gently pressed down to keep them inside the Kapton wells. Shock compression experiments were performed only after the water in the sample paste was vacuumed off using specially designed grooves in the sample holder, leaving a flat, compact, cylindrical volume of cryptomelane in the wells. Control experiments were performed on (1) loose powdered, (2) wet paste, and (3) initially wet but finally dry compact samples. While presence of water cannot be completely ruled out, it is more likely that the samples were dry at that point. Postmortem spectroscopy and microscopy were performed on completely dried samples by waiting for at least 48 h after the shock compression experiments were performed. There was no difference in the postmortem Raman and microscopy data from the three types of samples used in control experiments. However, significantly less volume of shocked cryptomelane was recovered when #1 and #2 methods were applied for sample mounting, making the overall analysis more challenging. All experiments reported in this report have used the method #3.

Shock Compression Experiments

The shock compression experiments described here employed an inverted shock microscope where laser driven flyer plates are used. The apparatus was developed and thoroughly characterized by the Dlott research group [34–36]. The diagnostics of the system were reported previously to establish the reliability and precision of the laser-driven flyer plates as a scientific tool for novel dynamic compression experiments [34–39]. The shock compression apparatus uses a high-energy laser to launch tiny discs of metal, which then travels at high velocities before impacting a sample, thereby compressing it. The pressure applied to the sample is precisely linked to the impact velocity of the flyer. Figures 2 and 3 present an overview of the shock compression apparatus. A Nd:YAG laser (Spectra-Physics Quanta-Ray Pro-350-10) of wavelength 1064 nm, with a maximum pulse energy of 2.5 J, pulse width of 20 ns, and a high value of $M^2 = 40$ is used as the launch laser. The flyer plates are generated from Al 1100 foils epoxied to Pyrex (glass) plates either two or three inches square and 6.35 mm thick. Each flyer is a disc of 0.5 mm diameter, moving with its flat surface parallel to the sample plane. Due to the hypervelocity impact, the flyer sends a shock wave into the sample. Several kinds of foils
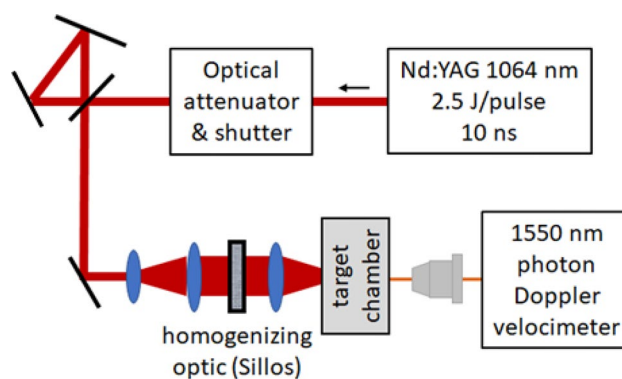

Fig. 2 Schematic of the shock compression microscope with laser launched flyer plates. The sample and the flyer plate assembly is inside the target chamber. The details of the target chamber are shown in Fig. 3
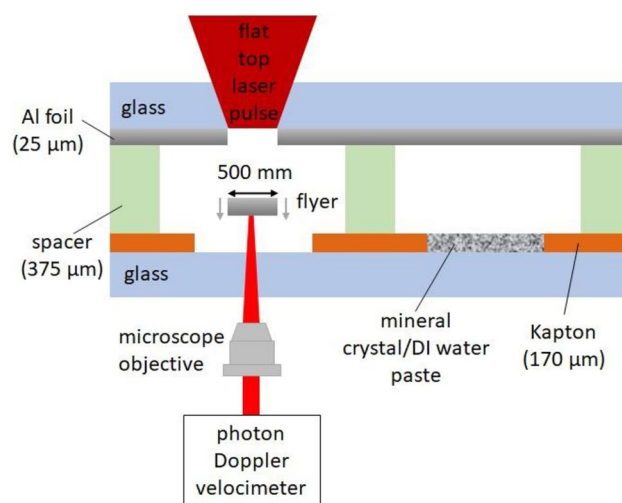

Fig. 3 Schematic of target chamber illustrating two different sample configurations using Kapton films to create microcuvettes. The left configuration shows a laser launched flyer moving towards a glass substrate with a photon Doppler velocimeter tracking the flyer. On the right, a mineral sample configuration is displayed. By moving the launch laser to the right, a new flyer can be launched to impact the mineral sample, thereby sending a shock wave through it

could be used, including Al, Cu, and stainless steel. However, the most commonly used materials are Al foils with 25, 50, or 75 µm thicknesses. The choice of material and thickness depends on sample characteristics such as reactivity, initiation threshold and optical parameters. The flyer velocities could be precisely controlled through laser power, and the shock duration are controlled through the foil thickness. The setup is versatile to accommodate solids and liquids. The samples are mounted inside a target chamber with the launch laser coming in from one end and several measurement probes are connected at the other end. Solid samples can be shock compressed under vacuum using specially

designed vacuum grooves in the sample mount. Typically, the flyer velocities, and hence the pressures, are determined by a photon Doppler velocimeter (PDV) synchronized to the system. However, for opaque samples when there is no direct recording of the velocity histories, pressures are estimated through flyer experiments on glass.

The shock compression experiments in cryptomelane were performed using 20 ns pulse duration with 1 J of pulse energy on 25 μm Al 1100 flyers with 3.5 km/s impact velocities to produce planar shock waves of 5 ns duration in the sample. The reproducibility in flyer velocities ($\pm 0.56\%$) as well as impact times ($\pm 0.59\%$) were demonstrated previously [35, 36, 45]. Figure 4 presents examples of flyer impact experiments on Pyrex adapted from Bhowmick et al., as evidence of consistent flyer speeds, duration of compression, shot to shot variability of flyer speeds, and impact times.

Since cryptomelane was opaque to the 1550 nm PDV beam, no velocity history could be recorded for the actual experiments where Al flyers impacted cryptomelane samples. However, experiments with Al flyers and glass (Pyrex) were performed to ensure the flyer speed of 3.5 km/s and to comment on the uncertainties related to flyer speed quoted in this work. A total of 10 shots were taken to confirm the Al flyer speed on glass. These experiments returned a flyer speed of 3.5 km/s ± 0.03 km/s through standard deviation. The window correction index $n_c = 1.0627$ [35] was used in calculation of PDV velocity histories to all control experiments. A representative velocity history from Al flyer on glass is presented in Fig. 4d. It should be noted that the window correction index introduces an uncertainty of 1% to the velocities for several km/s, and hence should not be a major source of errors [35]. It could be concluded that all the single shot experiments in cryptomelane were performed under the same conditions. A total of 50 shots were conducted on cryptomelane samples, all with the same flyer speed. The spectroscopic data presented here are representative from multiple trials. Shock velocities (U_s) in any media are generally obtained from the shock Hugoniot equations. In many cases, the equation represents a straight line given in the form:

$$U_s = A + B * U_p$$

where U_s is shock velocity, U_p is particle velocity, A is the speed of sound in the material, and B is the slope of the line. Al 1100 has an average density of 2.712 g/cm³ with a Hugoniot equation given by $U_s = 5.38 + 1.34\ U_p$ [46]. Neither experimental, nor theoretically calculated shock Hugoniot information for cryptomelane was available. As an alternative, the pyrolusite Hugoniot data could be taken to estimate pressures, since pyrolusite (4.318 g/cm³) and cryptomelane (4.35 g/cm³) have similar densities. The shock Hugoniot equation for pyrolusite reported in "LASL Shock Hugoniot Data" report (Marsh (ed.)) has cumulative experimental work [47], 48, and is given by:

$$U_s = 3.77 + 1.46 * U_p$$

Using pyrolusite density, a flyer velocity of 3.5 km/s from control experiments, and via impedance matching between Al flyer and pyrolusite targets, the pressure was

Fig. 4 Repeatability of flyer plate velocities and impact times, with an example of control experiment performed by Al flyer on glass. On the left panel **a**, several flyer impact examples are included between $U_f = 1$–4 km/s, where the impact (time = 0 ns) is followed by a 5 ns flat region, corresponding to shock duration in Pyrex, adapted from [35, 36]. On the right, flyer impact time consistency (**b**) and attained impact velocities for a fixed laser power are demonstrated (**c**), adapted from [35, 36]. The plot presented in **d** is a representative experiment out of 10 shots launched to calibrate impact speed where an Al flyer is impacting glass (Pyrex) without any cryptomelane present
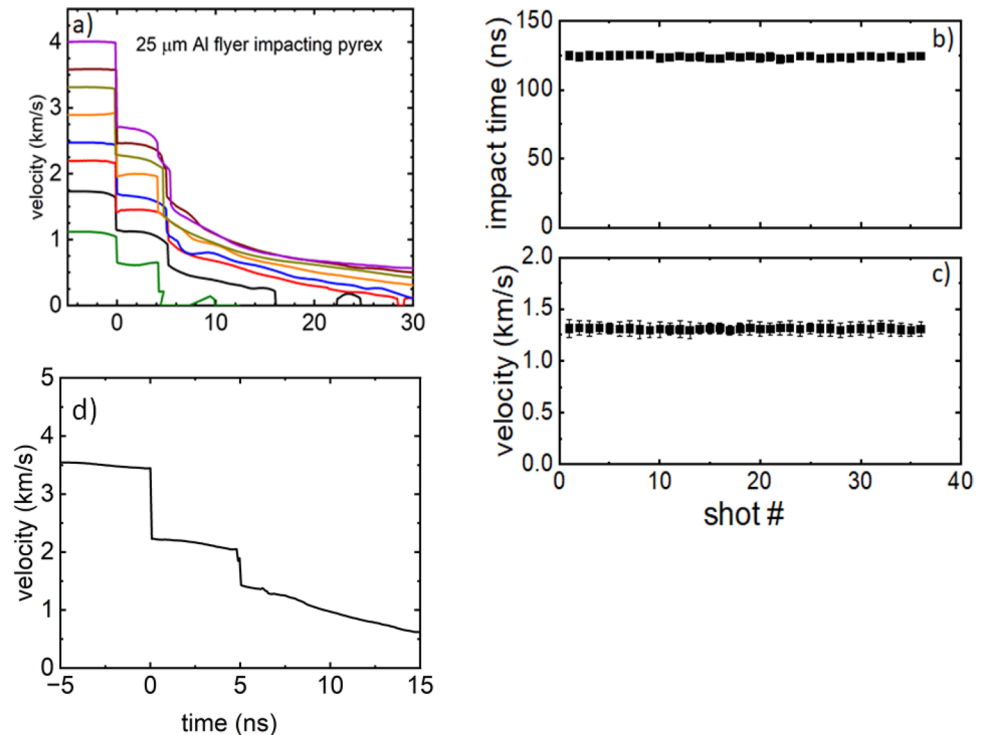
calculated to be ~ 41.4 GPa. Another alternative could be to use a linear Hugoniot ($U_s = 3.61 + 1.47 * U_p$) reported for epoxy-MnO_2 composite [49]. Using a density for epoxy-MnO_2 of 2.6 g/cm^3, with the impedance matching technique, an estimated ~ 32.1 GPa pressure was found. It is reasonable to assume that all shock compression experiments in cryptomelane were performed at a pressure between 32.1 and 41.4 GPa. Considering the densities, it is more likely that the pressure is close to the estimated value of 41.4 GPa. Avoiding further speculation, and to include the high degree of uncertainty in the Hugoniot EOS, the mean pressure from the two calculations with a standard error as our applied pressure in these experiments. This is 36.8 GPa $\pm$ 4.7 GPa. This value is reasonable since in mineral groups such as feldspars, the same flyer velocity projects a pressure between 20 and 40 GPa [50].

A challenge to perform high-throughput spectroscopy under shock is that each single shot experiment destroys the sample. Hence these experiments used a versatile and inexpensive sample array designed and characterized previously [35–38]. An overview of the sample array is presented in Fig. 3, where hundreds of laser-milled microcuvettes are seen on a polyimide or Teflon adhesive tape put onto a glass substrate, with the sample thickness is determined by the thickness of the tape.

X-ray Diffraction

Powder X-ray diffraction was performed on both starting material and post-shock recovered material using a Bruker D8 Advance powder X-ray diffractometer, in order to confirm the phase of the material and to observe any changes to main peak shapes or positions. Data on both samples were collected from 4° 2θ to 70° 2θ, with a step size of 0.02° 2θ at 0.1 s per step using Cu radiation (0.15418 nm wavelength). Powders were mounted on "zero" background holders themselves which are cut 6° off the c-axis of synthetic quartz. Accompanying Bruker software DiffracEva and the Powder Diffraction File (PDF) database were used for phase identification including PDF card # 01-072-1982 (tetragonal (I $\frac{4}{m}$) K-cryptomelane).

Electron Microscopy

Scanning electron microscopy (SEM) investigation was performed with a Zeiss Supra 35 VP electron microscope using a field-emission gun (FEG), an energy-dispersive X-ray spectrometer (EDS), and a backscatter electron detector. Round 12.7 mm SEM aluminum stubs with conductive carbon tabs were used to mount loose granular material and detached foil with experimental charge. The instrument was used in both backscatter electron (BSE) and variable-pressure modes for imaging. Nitrogen (N_2) was used as the compensating gas for variable-pressure mode and the voltage used was 25.kV. Previous investigations have used this instrument in a similar manner for cryptomelane specifically (i.e., [8, 44]) and several publications have used this instrument in similar conditions for other oxides or complex materials (e.g., [51–61]).

For transmission electron microscopy (TEM) investigation a small amount of sample was suspended in approximately 2 mL of ethanol in a glass vial and vigorously shaken and allowed to settle for 30 s. An aliquots of approximately 5 μL was then placed onto a 3-mm copper grid with lacey-carbon film and allowed to air dry. A JEOL JEM-2100 transmission electron microscope that was operated at 200 kV and equipped with a Bruker EDS detector was used for bright-field imaging and chemical analysis. Images were taken with a Gatan Orius SC 200D CCD camera. Selected-area electron diffraction (SAED) patterns were used to determine crystallinity characteristics. Similar approaches using this instrument have been published in previous investigations of cryptomelane [8] as well as other materials (e.g., [57, 59, 62–65]).

For EDS the lines used to identify elements provided by Bruker software include O-K = 0.525 keV; Na-K 1.040 keV; Al-K = 1.487 keV; Si-K_α = 1.740 keV (nominally K_β = 1.837 keV); K-K_α = 3.312 keV and K-K_β = 3.590 keV; Mn-K_α = 5.895 keV and Mn-K_β = 6.492 keV; and Cu-K_α = 8.036 keV and Cu-K_β = 8.903 keV; Carbon sticky tabs, the ubiquitous nature of O, and Al stubs may contribute to some of the EDX spectra for SEM data. The ubiquitous nature of O and scatter from the Cu grid and the lacey-C substrates contribute to TEM–EDX spectra.

Raman Spectroscopy

To investigate any permanent impact of compression on molecular structure of cryptomelane, we collected Raman spectra from unshocked and shocked samples recovered after the experiments. The post-mortem Raman analysis was performed on a confocal Raman microscope (Horiba LabRam HR) with a 100×/0.95NA objective and a 633 nm excitation laser. Each spectrum was collected from an area of 1 μm in diameter with an acquisition time of 5 s and 3 averages.

Results

Powder X-ray Diffraction

Figure 5 provides triplicate examples of powder X-ray diffraction patterns of shocked cryptomelane and starting material. Comparison of powder diffraction data to PDF card # 01-072-1982 confirms that both the starting material and recovered material were predominantly tetragonal
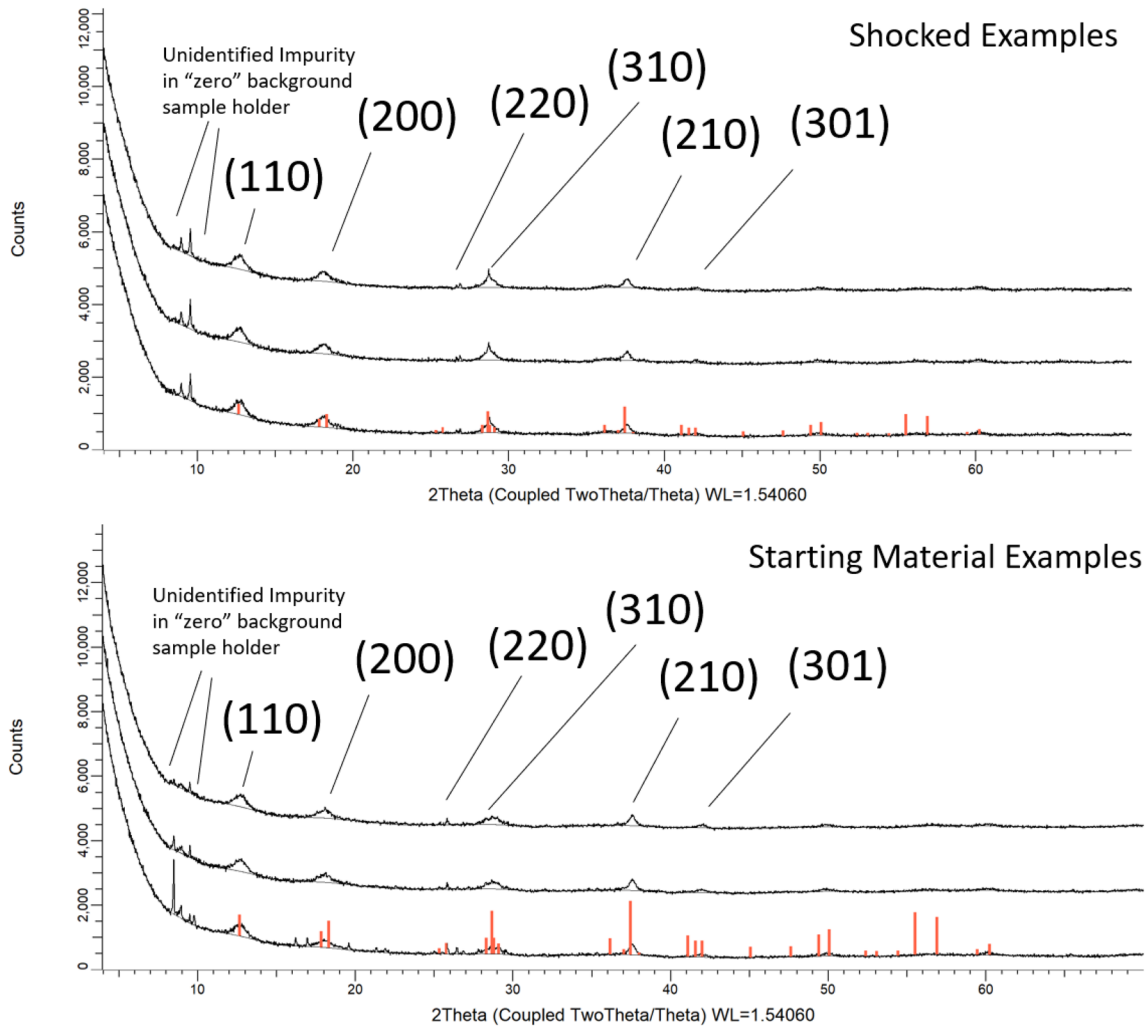
Fig. 5 Powder X-ray diffraction patterns for starting material and shocked materials. Unidentified impurity is from the "zero background" plate and this was manufacturer error the peaks do not overlap with cryptomelane and TEM indicated no major additional phase was produced in shock

(I $\frac{4}{m}$) K-cryptomelane. This was done by matching the major reflections and d-spacing values of $d_{(110)} = 6.91$ Å, $d_{(200)} = 4.89$ Å, $d_{(310)} = 3.10$ Å, and $d_{(211)} = 2.39$ Å. Peak positions measurements show that there is little to no peak shift from unshocked to shocked cryptomelane, however full peak width at half peak maximum (FWHM) values show there are observable changes (Table 1). Sharpening is observed most prominently for (310) with the average (n = 3) FWHM values for unshocked (310) reflections decreasing 35%.

Table 1 XRD peak characteristics of cryptomelane K-OMS-2 for starting material and post-shock conditions

Reflection	Starting (FWHM)	Shocked (FWHM)	Sharpened post shock	Broadened post shock
{110}	0.610	0.629	No	0.019 (3%)
{200}	0.637	0.656	No	0.019 (3%)
{310}	0.392	0.254	0.138 (35%)	No
{211}	0.410	0.359	0.051 (12%)	No
{301}	0.173	0.023	0.15 (86%)	No
{411}	0.146	0.202	No	0.056 (38%)
{521}	0.129	0.144	No	0.015 (11%)

FWHM values for shocked (301) also decreased indicating peak sharpening with the average (n = 3) FWHM values for unshocked (301) reflections decreasing 86%. Broadening occurred post shock for (411) by 38% and negligible (3%) to minor (~ 12%) broadening occurred for (110), (200), (521). There are two additional sharp low-2θ angle peaks in both data sets that are inherent to the "zero" background quartz plate holder that each powder was mounted on for diffraction; separate tests on empty quartz plates have confirmed that this is the source of the reflections and that there are none which would overlap with the cryptomelane K-OMS-2 pattern.

Scanning Electron Microscopy

Scanning electron microcopy work focused on areas of removed foil material to determine whether or not cryptomelane or other phase were present at the mesoscale and observed textures (Fig. 6). Coherent aggregates of cryptomelane crystals were commonly observed in 90% of sample (Fig. 6a) and had typical radial acicular to bird's nest textures consistent with starting material (e.g., [8]). Cryptomelane crystals observed were euhedral and were approximately 1 to 3 μm and approximately 100 to 400 nm in width. The other primary texture observed which was less common (10%) was well rounded, smooth-surfaced spherules that had lower contrast than the aluminum foil in which they occurred (Fig. 6b). These particles had diameters that varied from approximately 10 μm to 100 nm in diameter and had a relatively even distribution in what appears to be potentially quenched Al foil (Fig. 6c). Many of these spherules were embedded in the matrix of the Al foil and EDS spectra

from them showed a relative enrichment of Mn relative to K. Owing to the nature of the spherules being embedded in the Al foil substrate, it is unclear whether or not Al is inherent to the spherules or is simply background from the foil.

Transmission Electron Microscopy

Transmission electron microscopy on starting material is consistent with the observations of Cymes et al. [8]. Cryptomelane occurs dominantly as typical radial acicular to bird's nest aggregate textures. Aggregates of starting material have high internal nanoporosity which is visually estimated to be between 10 and 40% of the volume of aggregates. Approximately 95% of aggregates have some radial to random crystal orientation (Figs. 7, 8). Selected area electron diffraction of these aggregates yields diffraction rings consistent with the spacings of cryptomelane and have well defined diffraction spots with only minor amounts of streaking (Fig. 7a). Cryptomelane crystals in the starting material are euhedral and crystalline and single crystals are commonly 15 to 100 nm in width and approximately 300 nm to 2 to 3 μm in length. Individual crystals are characterized by continuous coherent lattice fringes (Fig. 7b) and have single net diffraction patterns.

Transmission electron microscopy on shocked material has the same textures of aggregates with typical radial acicular to bird's nest aggregate textures. Aggregates of shocked material retain a high internal nanoporosity which is visually estimated to be unchanged from that of the starting material. The aggregates observed also have the same radial to random crystal orientation (Fig. 9). The particle size of the cryptomelane also appears to be approximately the same
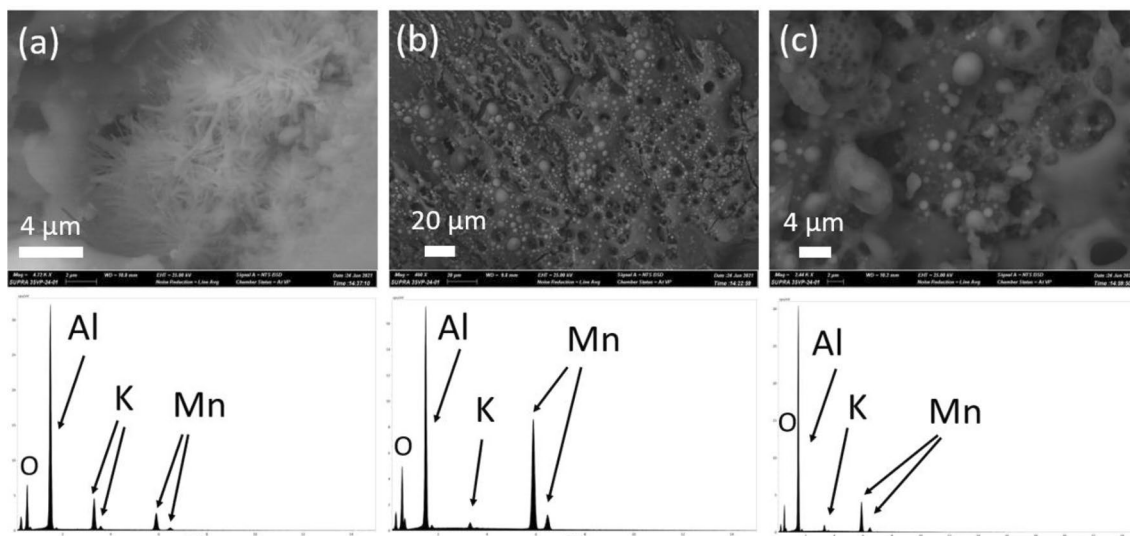

Fig. 6 Scanning electron microscopy images with paired EDS spectra below. **a** shows intact shocked cryptomelane crystals that were typical of the sample. **b** shows fewer common spherules embedded in Al foil with K and Mn with **c** being a higher magnification image
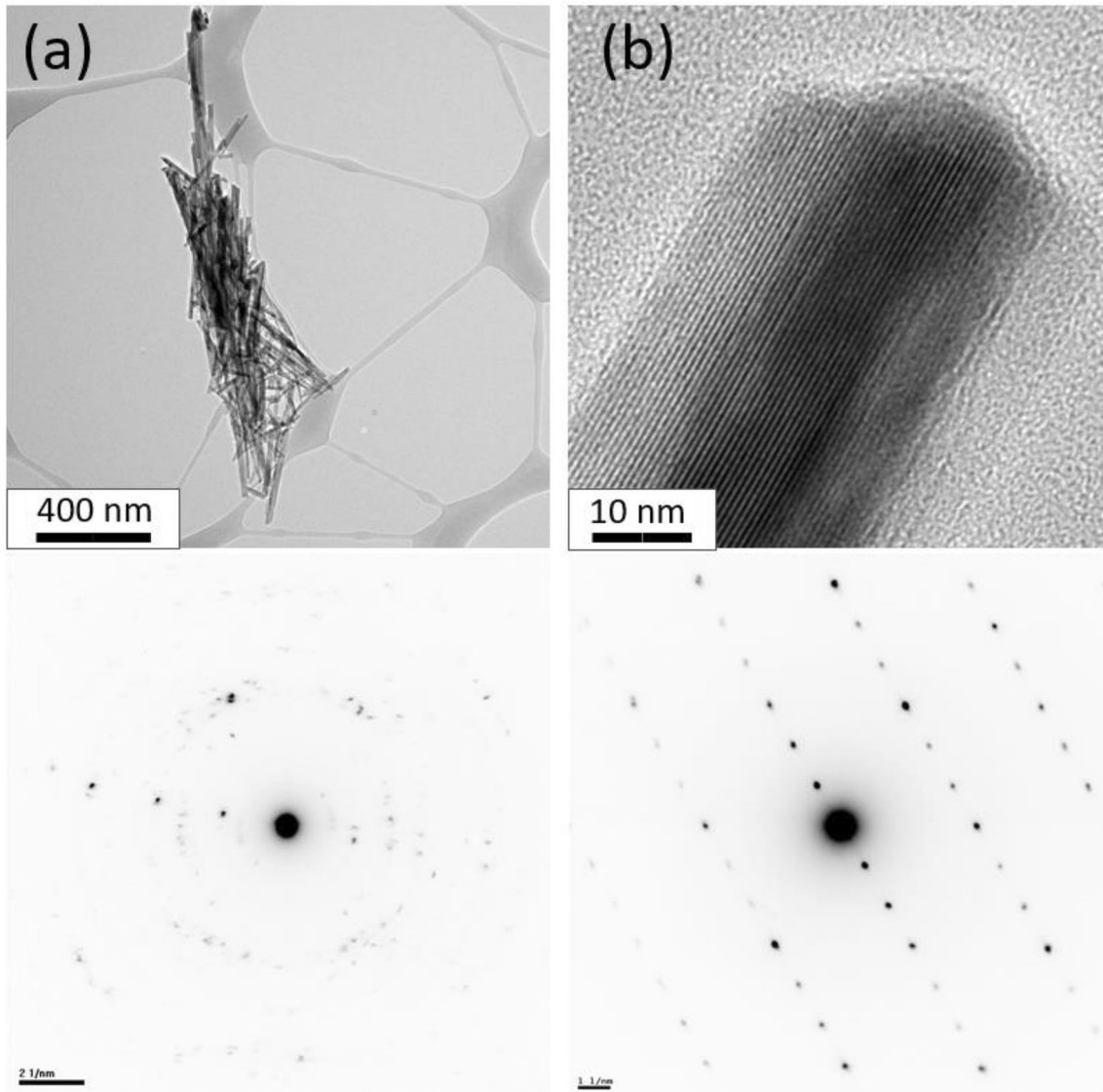
Fig. 7 a Bright field TEM image of an aggregate of cryptomelane from the starting material showing euhedral crystals in a radial aggregate to bird's nest texture exhibiting abundant nanoporosity. This aggregate exhibit alignment of crystals in the upper portion and more random orientation in the lower portion. The SAED data below shows that these particles have reasonably well-formed spots and spots conform to positions expected of I4/m cryptomelane along ~[h0l]. **b** and example of an individual fiber in the starting material showing coherent lattice fringes and a single net of well-formed diffraction spots

and there are no examples of small fragments of nano crystals or amorphous material generated from shock. Selected area electron diffraction of these aggregates yields diffraction rings consistent with the spacings of cryptomelane however there is much more pronounced streaking in all reflections (Fig. 9). Cryptomelane crystals in the shocked material appear to be largely crystalline. Individual crystals appear to exhibit retain intergrowth or adhesion more than in the shocked materials (Fig. 9). These fiber aggregates also exhibit comparatively more streaking in diffraction patterns compared to single crystals in the starting material and undulations at the crystal face with approximately 0.5 to 1.0 nm of relief are observed. Continuous coherent lattice fringes are commonly observed but examples of slightly distorted lattice fringes also occur (Fig. 10). The streaked diffraction, surface undulations, and distorted lattices observed in the TEM data are interpreted to be the result of shock.

Spectroscopy

Figure 11 presents the comparison of representative spectra, where we can see the expected 180, 570, and 641 cm^{-1} in the unshocked spectra, as have been reported in cryptomelane before (e.g., [66]). The sharp low frequency band at
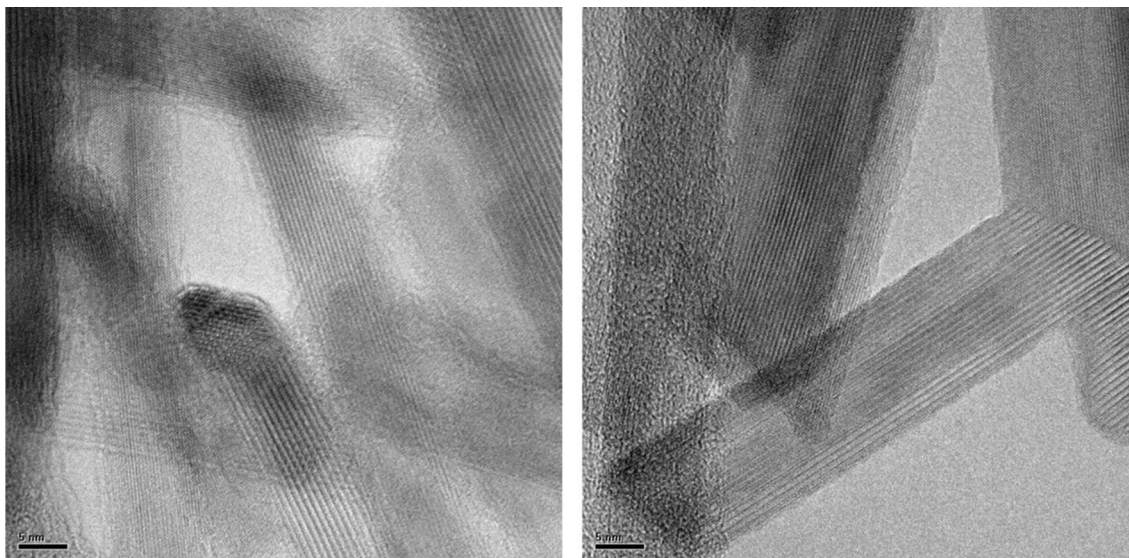
Fig. 8 Bright field images of starting material cryptomelane showing euhedral crystal faces and the nature of nanopores. Left image shows one small crystal partially imaged along ~[001] on the lower portion of a nanopore. Lattices are evident in crystals and the variation is interpreted to be in part form differences of the sample off of the focal height. Right image shows an additional example of euhedral crystal faces and a nanopore as well as an intergrowth of cryptomelane crystals. Lattices demonstrate continuity along [001]. Amorphous material on the left is lacey carbon
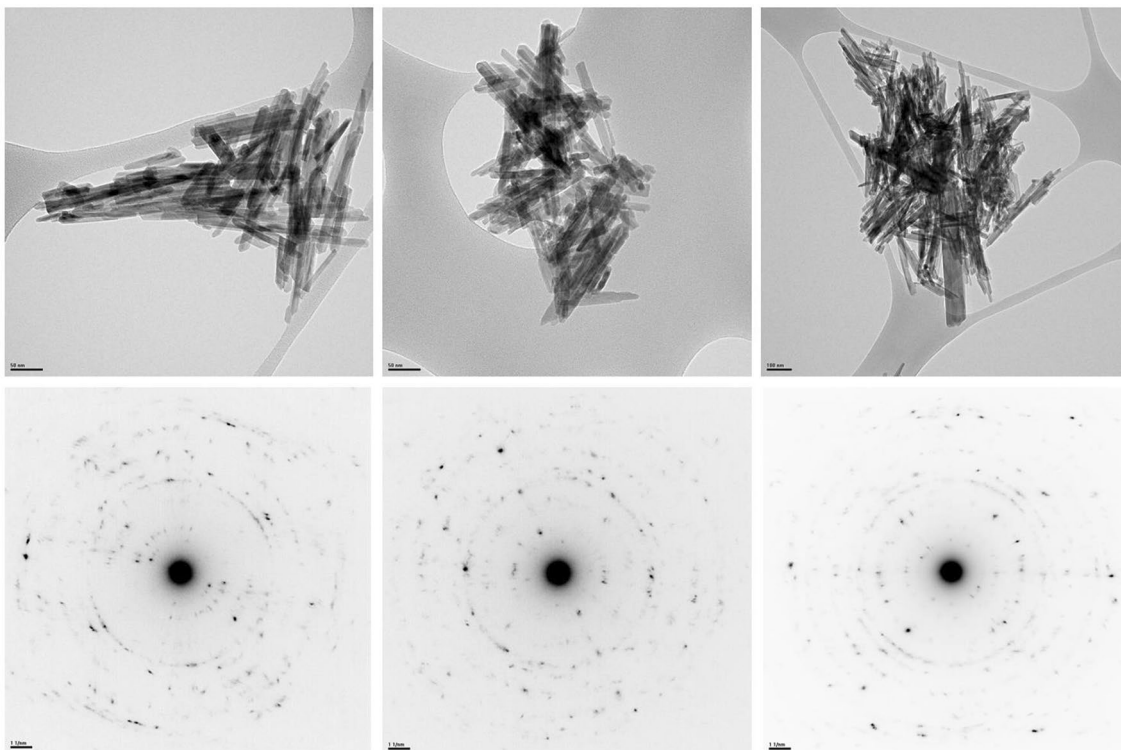

Fig. 9 The top row shows bright field TEM image of aggregates of cryptomelane from shocked material paired with electron diffraction data of each. These images show apparently intact radial aggregate or bird's nest textures and also exhibit abundant nanoporosity. These aggregates show random orientation of crystals and the SAED data below shows that these particles have diffraction spots that are moderately to extensively streaked. Spots conform to positions expected of cryptomelane
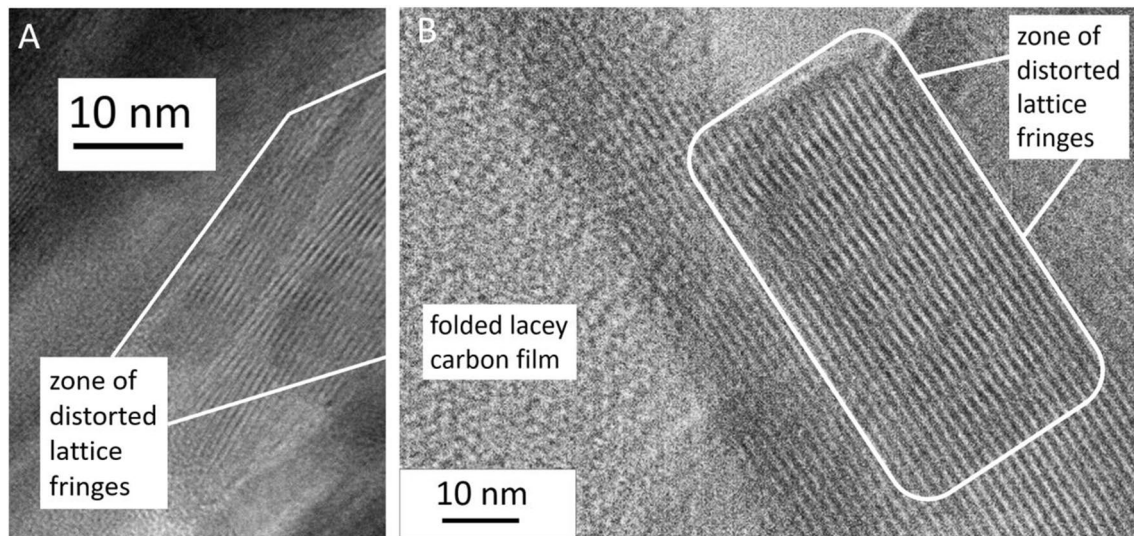
Fig. 10 Lattice images showing distortion along ~[001] with a wavelike modulation approximately 5 to 10 nm in periodicity. These features are interpreted as the result of shock deformation

180 cm^{-1} is assigned to the translational motion of MnO$_6$ octahedra, while the 570 and 641 cm^{-1} bands correspond to the symmetrical vibrations of oxygen atoms with respect to Mn atoms and Mn–O stretching modes in the direction orthogonal to the double chains of the MnO$_6$ octahedra. The sharp bands of 570 and 641 cm^{-1} also confirm well-developed tetragonal cryptomelane structure with an interstitial space comprising of (2×2) tunnels. Interestingly, the bending vibration of 383 cm^{-1}, and the 505 cm^{-1} symmetrical vibration bands were extremely weak, and thus are barely recognizable in the scale of the plot. The Raman modes in the recovered cryptomelane after the compression experiments show some interesting features. The sharp band at 180 cm^{-1} remains intact without change in intensity. Both the symmetric stretch bands of 570 and 641 cm^{-1} wavenumbers show frequency shifts, with their relative intensity inverted. Figure 11 shows the band shifting and the intensity change clearly. The 570 cm^{-1} band shifted slightly towards higher frequency while the 641 cm^{-1} band shifted a significant amount towards lower frequency. It is clear from the Raman spectra that shocking has altered the structure of cryptomelane, where the 570 cm^{-1} band-shift probably corresponds to a slight decrease in bond length.

The inversion of the Raman peaks at 570 cm^{-1} and 641 cm^{-1} indicates possible structural changes, broadly analogous to those observed in MnO$_2$ phases (e.g., [67]). The change of the relative intensities of the Raman peaks indicates the material underwent a permanent phase transition under shock compressions, while the peak shifts demonstrate the changes in the length of chemical bonds. The peak at 570 cm^{-1} is attributed to the Mn–O stretching in the basal plane of the MnO$_6$ sheet, while the peak attributed to the symmetric stretching vibration of Mn–O of the MnO$_6$ groups [68]. Therefore, the redshift of peak from 570 to 575 cm^{-1} indicates the shortening between the distance of one MnO$_6$ layer with respect to the next, while the significant blueshift of the peak from 641 to 625 cm^{-1} indicates the stretching of Mn–O bond within the MnO$_6$ layer.

Discussion

Phase Identification

TEM imaging suggests some degree of formation of amorphous regions at and near the surfaces of shocked cryptomelane. At the TEM scale, there are no indications of formation of secondary phases such as spinels (e.g., hausmanite) or other high-pressure phases resulting from transformation. Although there are clear indications of deformation in diffraction data and images, cryptomelane persists under these shock conditions. At the TEM scale, discrete particles of glass or amorphous material was also not observed in shocked samples indicating that mass of the shocked minerals appears to be largely intact and not redistributed or broken. The spherules observed embedded in Al foil may be dominantly Al droplets from melting that may have some inclusions of cryptomelane, may be Mn- and Al-rich oxides or other minerals. Although present, these spherules are not the dominant phase (~ 10%) at the mesoscale or nanoscale.

XRD data indicates that shocked material is crystalline, has diffraction peaks that are at the same position and perhaps counterintuitively, has a major increase in FWHM values for some major reflections and exhibits some peak
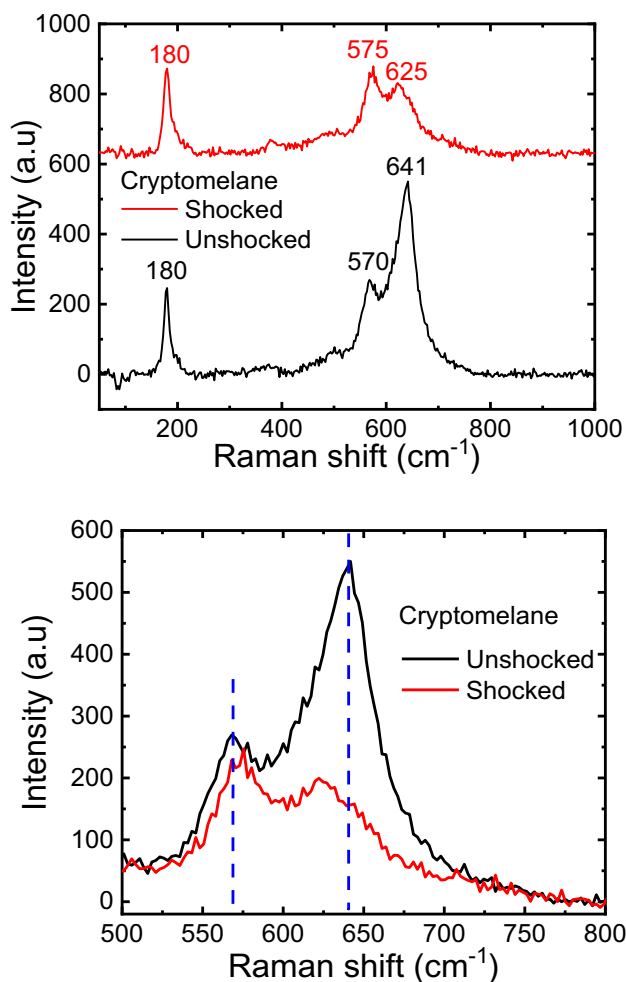
Fig. 11 (Upper spectra) Comparison of Raman spectra in unshocked (bottom) and shocked (top) cryptomelane. (Lower spectra) Band shifting, intensity change, and peak broadening in shocked cryptomelane

broadening for others. There appears to be no clear systematic relationships between those reflections that show broadening and those that show sharpening of peaks, however the peaks showing the most sharpening have hkl values with $h = 3$ and this relates to Mn cation positions. This increase in sharpening is interpreted as a relative increase in crystallinity of the material but the fundamental cause remains unclear. TEM data shows that the size of particles remains unchanged and thus the observed differences in FWHM are not from an enlargement of crystal size which hypothetically may be an explanation considering Scherrer formula particle size effects (e.g., [69]).

Proposed Mechanism

TEM data indicates that cryptomelane retains its overall texture as intergrown aggregates of nanoscale crystals that are elongated fibers with aspect ratios commonly > 20, and these aggregates have a relatively high percentage of nano-porosity. Thus, there is a high proportion of pores which by visual estimation varies between 10 and 40%. These pores occur largely in a uniform fashion in the aggregates. The pores may act as accommodation space for crystals to move, align, and rebound in a thixotropic fashion during shock. This may attenuate the propagation of shock in the solid state. The amorphous rinds or regions that appear in shocked crystals near former crystal faces, and more crystalline regions interior to the particles support this interpretation as particle–particle collision and interaction with atmospheric gasses filling the pores would be expected to impart more energy (higher temperatures, shock, and diffusion of oxygen). Diffusion of gaseous oxygen into cryptomelane structure is a well-recognized process and is related to the Mars and Van Krevelen mechanism (e.g., [70]) and thus the amorphous texture observed may reflect shock infusion of oxygen into the crystal structure at elevated temperatures. A highly energetic infusion of oxygen at the surface of the crystals would hypothetically reduce crystallinity and the limited concentration of oxygen in the nanopores may be a limiting factor in such a hypothetical reduction in crystallinity. In the future this could be tested using a pure oxygen environment with the expected result to be a reduction in crystallinity owing to rapid diffusion of comparatively more oxygen into the structure.

Also to be considered is the collapse and potential rebound of the channels in the structure and it is possible that the amorphous rinds observed reflect such a process well. The extent and nature of tunnel collapse and rebound should be investigated in future work and potential insight could be gained by extensive comparative studies of Mn-oxides with varying tunnel morphology (e.g., romanechite, todorokite) or studies of other tunnel structures such as akaganéite.

There is no clear mechanism that completely explains the shock resistance of cryptomelane however a thixotropic model where cryptomelane crystals move, are more aligned and then rebound seems plausible. The factors that influence the quality of this process such as nanopore size and distribution, diffusion of oxygen and other ambient gasses, and orientation of cryptomelane crystals in starting material aggregates are all factors to be explored in further investigations.

Implications for Future Work

Owing to the fine particle size of the material, it was very unexpected that cryptomelane would be shock resistant rather than transform into other phases. Accordingly, this investigation opens a wide range of questions regarding the stabilities of shocked cryptomelane and similar minerals.

The effect of substitution of cations, the size shape and orientation of particles, the nature and distribution of nanoporosity should be further explored in the hollandite structures. Whether or not atmospheric oxygen diffuses or exchanges with cryptomelane during shock should be investigated. Furthermore, whether other fibrous manganese oxides such as ramsdellite, romanechite, and todorokite, exhibit shock resistance should be investigated to explore systematic structural relationships. Additionally, other fibrous minerals such as palygorskite, sepiolite, and goethite should be investigated to determine if these minerals exhibit any shock resistance. Shock resistant properties of minerals may have general engineering and product implications.

Conclusions

Unexpectedly, cryptomelane is shock resistant as confirmed by TEM and XRD data and there is minimal redistribution of mass into other mineral or glass phases. Shock effects include deformation of some lattices, streaking of electron diffraction, formation of amorphous zones near crystal surfaces, and an apparent sharpening of bulk powder X-ray diffraction data. The proposed mechanism for shock resistance is related to a possible thixotropic collapse and rebound phenomenon enabled by significant nanoporosity in the material and the particle texture. The shock resistant property of cryptomelane opens new questions regarding the fundamental properties and applications of this and other related materials.

Data availability Data will be made available upon request.

Declarations

Conflict of interest All authors declare that there is no conflict of interest, real or perceived by any and all authors. Dr. Mark Krekeler is signing on behalf of all authors.

References

1. Birkner N, Navrotsky A (2017) Thermodynamics of manganese oxides: sodium, potassium, and calcium birnesite and cryptomelane. Proc Nat Acad Sci 114:1046–1053. https://doi.org/10.1073/pnas.1620427114

2. Lucht KP, Mendoza-Cortes JL (2015) Birnessite: a layered manganese oxide to capture sunlight for water-splitting catalysis. J Phys Chem C 119:22838–22846. https://doi.org/10.1021/acs.jpcc.5b07860

3. Grangeon S, Bataillard P, Coussy S (2020) The nature of manganese oxides in soils and their role as scavengers of trace elements: implications for soil remediation. In: van Hullebusch ED, Huguenot D, Pechaud Y, Simmonnot MO, Colombano S (eds) Environmental soil remediation and rehabilitation. Springer, Cham, pp 399–429. https://doi.org/10.1007/978-3-030-403485_7

4. Zhang S, Livi KJT, Gaillot A-C, Stone AT, Veblen DR (2010) Determination of manganese valence states in (Mn3+, Mn4+) minerals by electron energy-loss spectroscopy. Am Mineral 95:1741–1746

5. Post JE, Von Dreele RB, Buseck PR (1982) Symmetry and cation displacements in hollandites: structure refinements of hollandite, cryptomelane and priderite. Acta Cryst B 38:1056–1065. https://doi.org/10.1107/S0567740882004968

6. Awaluddin A, Astuti L, Linggawati A, Siregar SS, Prasetya P, Saputra L (2018) The Cu-doped cryptomelane-type octahedral molecular sieve manganese oxide synthesized by sol-gel for the degradation of methylene blue. AIP Confer Proc. https://doi.org/10.1063/1.5065035

7. Ching S, Roark JL, Duan N, Suib SL (1997) Sol-gel route to the tunneled manganese oxide cryptomelane. Chem Mater 9:750–754. https://doi.org/10.1021/cm960460k

8. Cymes BA, Almquist C, Krekeler MPS (2020) Europium-doped cryptomelane: multi-pathway synthesis, characterization, and evaluation for the gas phase catalytic oxidation of ethanol. Appl Catal A 589:117310. https://doi.org/10.1016/j.apcata.2019.117310

9. DeGuzman RN, Shen YF, Neth EJ, Suib SL, O'Young CL, Levine S, Newsam JM (1994) Synthesis and characterization of octahedral molecular sieves (OMS-2) having the hollandite structure. Chem Mater 6:815–821. https://doi.org/10.1021/cm00042a019

10. Ding Y, Shen X, Sithambaram S, Gomez S, Kumar R, Crisostomo VMB, Steven L, Suib SL, Aindow M (2005) Synthesis and catalytic activity of cryptomelane-type manganese dioxide nanomaterials produced by a novel solvent-free method. Chem Mater 17:5382–5389. https://doi.org/10.1021/cm051294w

11. Legutko P, Pęza J, Rossi AV, Marzec M, Jakubek T, Kozieł M, Adamski A (2019) Elucidation of unexpectedly weak catalytic effect of doping with cobalt of the cryptomelane and birnessite systems active in soot combustion. Top Catal 62:599–610. https://doi.org/10.1007/s11244-019-01132

12. Mo NT, Cam LM (2019) Stability of Cu-doped manganese oxide catalyst in the oxidation of m-xylene. Russ J Phys Chem A 93:2016–2022. https://doi.org/10.1134/s0036024419100182

13. Muya RK, Achola L, Njagi EC, Ombaka O, Suib SL (2019) Synthesis, characterization and applications of transition metal-doped manganese oxide catalysts. J Reas Life Sci Bioinf Pharm Chem Sci 5:16–30. https://doi.org/10.26479/2019.0502.02

14. Said S, El Maghrabi HH, Riad M, Mikhail S (2018) Photo-catalytic selective organic transformations by Fe-doped octahedral molecular sieves (manganese oxide) nano-structure. J Asian Ceram Soc 6:169–181. https://doi.org/10.1080/21870764.2018.1480686

15. Stelmachowski P, Videla AHM, Jakubek T, Kotarba A, Specchia S (2018) The effect of Fe Co, and Ni structural promotion of cryptomelane (KMn8O16) on the catalytic activity in oxygen evolution reaction. Electrocatalysis 9:762–769. https://doi.org/10.1007/s12678-018-0488-9

16. Sun M, Yu L, Ye F, Diao G, Yu Q, Hao Z, Yuan L (2013) Transition metal doped cryptomelane-type manganese oxide for low-temperature catalytic combustion of dimethyl ether. Chem Eng J 220:320–327. https://doi.org/10.1016/j.cej.2013.01.061

17. Zhang Q, Luo J, Vileno E, Suib SL (1997) Synthesis of cryptomelane-type manganese oxides by microwave heating. Chem Mater 9:2090–2095. https://doi.org/10.1021/cm970129g

18. Deng H, Kang S, Ma J, Zhang C, He H (2018) Silver incorporated into cryptomelane-type manganese oxide boosts the catalytic oxidation of benzene. Appl Catal B 239:214–222. https://doi.org/10.1016/j.apcatb.2018.08.006

19. Ghande AR, Rebello JS, Figueiredo JL, Fernandes JB (2007) Manganese oxide OMS-2 as an effective catalyst for total oxidation of ethyl acetate. Appl Catal B 72:129–135. https://doi.org/10.1016/j.apcatb.2006.10.017

20. Luo J, Zhang Q, Huang A, Suib SL (2000) Total oxidation of volatile organic compounds with hydrophobic cryptomelane-type octahedral molecular sieves. Microporous Mesoporous Mater 35–36:209–217. https://doi.org/10.1016/S1387-1811(99)00221-8

21. Luo J, Zhang Q, Garcia-Martinez J, Suib SL (2008) Adsorptive and acidic properties, reversible lattice oxygen evolution, and catalytic mechanism of cryptomelane-type manganese oxides as oxidation catalysts. J Am Chem Soc 130:3198–3207. https://doi.org/10.1021/ja077706e

22. Peluso MA, Gambaro LA, Pronsato E, Gazzoli D, Thomas HJ, Sambeth JE (2008) Synthesis and catalytic activity of manganese dioxide (type OMS-2) for the abatement of oxygenated VOCs. Catal Today 133–135:487–492. https://doi.org/10.1016/j.apcatb.2010.07.007

23. Said S, Riad M, Helmy M, Mikhail S, Khalil J (2016) Preparation of nano-structured cryptomelane materials for catalytic oxidation reactions. J Nanostruct Chem 6:171–182. https://doi.org/10.1007/s40097-016-0192-3

24. Santos DF, Soares OS, Figueiredo JL, Pereira MFR (2020) Effect of ball milling on the catalytic activity of cryptomelane for VOC oxidation. Environ Technol 41:117–130. https://doi.org/10.1080/09593330.2018.1491639

25. Santos VP, Pereira MFR, Órfão JJM, Figueiredo JL (2009) Synthesis and characterization of manganese oxide catalysts for the total oxidation of ethyl acetate. Top Catal 52:470–481. https://doi.org/10.1007/s11244-009-9187-3

26. Zhang X, Ma Z, Song Z, Zhao H, Liu W, Zhao M, Zhao J (2019) Role of cryptomelane in surface-adsorbed oxygen and Mn chemical valence in MnOx during the catalytic oxidation of toluene. Phys Chem C 123:17255–17264. https://doi.org/10.1021/acs.jpcc.9b02499

27. Dlott DD (2011) New development in the physical chemistry of shock compression. Annu Rev Phys Chem 62:575–597. https://doi.org/10.1146/annurev.physchem.012809.103514

28. Chao ECT (1967) Shock effects in certain rock forming minerals. Science 156:192–202. https://doi.org/10.1126/science.156.3772.192

29. French BM, Short NM (1968) Shock metamorphism of natural materials. Mono Book Corp, Baltimore

30. Offield TW (1987) Shock effects in rocks and minerals. In: Encyclopedia of structural geology and plate tectonics. Springer

31. Shoemaker EM (1960) Penetration mechanics of high velocity meteorites, illustrated by Meteor Crater, Arizona. In: Internat Geol Cong, 21st Copenhagen Rept pt, vol 18, pp 418–434

32. Short NM (1966) Shock processes in geology. J Geol Educ 14:49–166. https://doi.org/10.5408/0022-1368-XIV.4.149

33. Wackerle J (1962) Shock-wave compression of quartz. J Appl Phys 33:922–937. https://doi.org/10.1063/1.1777192

34. Bassett W, Johnson BP, Salvati L, Nissen EJ, Bhowmick M, Dlott DD (2020) Shock initiation microscopy with high time and space resolution. Prop Exp Pyrot 45:223–235. https://doi.org/10.1002/prep.201900222

35. Bhowmick M, Nissen EJ, Dlott DD (2018) Detonation on a tabletop: Nitromethane with high time and space resolution. J Appl Phys 124:075901. https://doi.org/10.1063/1.5043540

36. Bhowmick M, Basset WP, Matveev S, Salvati L, Dlott DD (2018) Optical windows as materials for high-speed shock wave detectors. AIP Adv 8:125123. https://doi.org/10.1063/1.5055676

37. Nissen EJ, Bhowmick M, Dlott DD (2021) Shock-induced kinetics and cellular structures of liquid nitromethane detonation. Combust Flame 225:5–12. https://doi.org/10.1016/j.combustflame.2020.10.046

38. Nissen EJ, Bhowmick M, Dlott DD (2021) Ethylenediamine catalyzes nitromethane shock-to-detonation in two distinct ways. J Phys Chem B 125:8185–8192. https://doi.org/10.1021/acs.jpcb.1c04427

39. Zhou X, Miao YR, Shaw WL, Suslick KS, Dlott DD (2019) Shock wave energy absorption in metal–organic framework. J Am Chem Soc 141:2220–2223. https://doi.org/10.1021/jacs.8b12905

40. Ferroir T, Onozawa T, Yagi T, Merkel S, Miyajima N, Nishiyama N, Irifune T, Kikegawa T (2006) Equation of state and phase transition in $KAlSi_3O_8$ hollandite at high pressure. Am Mineral 91:327–332. https://doi.org/10.2138/am.2006.1879

41. Graham RA, Morosin B, Richards PM, Stohl FV, Granoff B (1981) Shock activation of catalysts. AIP Conf Proc 70:464. https://doi.org/10.1063/1.32898

42. Han J, Xu S, Sun J, Fang L, Zhu H (2017) Pressure-induced amorphization in the nanoindentation of single crystalline silicon. RSC Adv 7:1357. https://doi.org/10.1039/C6RA26094B

43. Sun Y, Wang L, Liu Y, Ren Y (2015) Birnessite-type MnO2 nanosheets with layers structures under high pressure: elimination of crystalline stacking faults and oriented laminar assembly. Small 11:300–305. https://doi.org/10.1002/smll.201400892

44. Almquist C, Krekeler MPS, Jiang L (2014) An investigation of the structure and catalytic activity of cryptomelane-type manganese oxide materials prepared by different synthesis routes. Chem Eng J 252:249–262. https://doi.org/10.1016/j.cej.2014.04.102

45. Brown KE, Shaw WL, Zheng X, Dlott DD (2012) Simplified laser-driven flyer plates for shock compression science. Rev Sci Instrum 83(10):103901. https://doi.org/10.1063/1.4754717

46. Marsh SP (ed) (1980) LASL shock Hugoniot data. University of California Press, Berkeley, p 317

47. Van Thiel M, Kusubov AS, Mitchell AC (eds) (1967) Compendium of shock wave data. Lawrence Radiation Laboratory (Livermore) report UCRL-50108

48. Birch F (1966) Compressibility; elastic constants. In: Clark SP Jr (ed) Phys. const, revised. The Geological Society of America Inc, New York, pp 153–159

49. Jordan JL, Dattelbaum DM, Sutherland G, Richards DW, Sheffield SA, Dick RD (2010) Shock equation of multi-phase epoxy-based composite (Al-MnO2-epoxy). Appl Phys 107:103528. https://doi.org/10.1063/1.3357314

50. Ahrens TJ, Petersen CF, Rosenberg JT (1969) Shock compression of feldspars. J Geophys Res 74:2727–2746

51. Argyilan EP, Avis PG, Krekeler MPS, Morris CC (2015) The origin of collapse features appearing in a migrating parabolic dune along the southern coast of Lake Michigan. Aeol Res 19:137–149. https://doi.org/10.1016/j.aeolia.2015.09.008

52. Armentrout C, Burke M, Silverstein J, Krekeler MPS, Nesbit L, Kidd M, Straub K, Newby N, Sellers A (2015) An unusual occurrence of silver in stream sediment from northern Breathitt County, Kentucky. Southeast Geol 51:109–119

53. Dietrich M, Wolfe A, Burke M, Krekeler MPS (2019) The first pollution investigation of road sediment in Gary, Indiana: anthropogenic metals and possible health implications for a socioeconomically disadvantaged area. Environ Int 128:175–192. https://doi.org/10.1016/j.envint.2019.04.042

54. Flett L, McLeod C, McCarty J, Shaulis B, Frain JJ, Krekeler MPS (2021) Providing environmental health contexts for Native American populations on the Spokane Reservation, WA: insights from tree bark particulate matter surrounding the Midnite uranium mine. Environ Res 194:110619. https://doi.org/10.1016/j.envres.2020.110619

55. Gawronska AJ, McLeod CL (2021) New insights into lunar magmatism: investigating open system processes in basaltic magma reservoirs on the Moon. In: Annual American Geophysical Union meeting, abstract 838758

56. Klein E, Krekeler MPS (2020) The occurrence of Hg, Se, S, Ni, Cr, and Th in talc ore: a scanning electron microscopy (SEM) study of historical samples from the Willow Creek Mine, Montana. Res Geochem 1:100003. https://doi.org/10.1016/j.ringeo.2020.100003

57. LeGalley E, Krekeler MPS (2013) A mineralogical and geochemical investigation of street sediment near a coal-fired power plant in Hamilton, Ohio: an example of complex pollution and cause for community health concerns. Environ Pollut 176:26–35. https://doi.org/10.1016/j.envpol.2012.12.012

58. Lindeman C, Oglesbee T, McLeod C, Krekeler MPS (2020) Mineralogy and geochemistry of the Kinnikinic Quartzite at the Arco Hills Silica and Gold Project in Butte County, Idaho: results of an ore quality spot check and implications for potential plasma furnace processing. Minerals 10:523

59. O'Shea M, Krekeler MPS, Vann DR, Gieré R (2021) Investigation of Pb-contaminated soil and road dust in a polluted area of Philadelphia. Environ Monit Assess 193:440. https://doi.org/10.1007/s10661-021-09213-9

60. Oglesbee T, McLeod C, Chappell C, Vest J, Sturmer D, Krekeler MPS (2020) A mineralogical and geochemical investigation of Modern Aeolian Sands near Tonopah, Nevada: sources and environmental implications. CATENA 94:104640. https://doi.org/10.1016/j.catena.2020.104640

61. Velázquez Santana LC, McLeod CL, Blakemore D, Shaulis B, Hill T (2020) Bolivian hornblendite cumulates: insights into the depths of Central Andean Arc magmatic systems. Lithos. https://doi.org/10.1016/j.lithos.2020.105618

62. Barnes M, McLeod C, Faraci O, Chappell C, Krekeler MPS (2020) Characterizing the geogenic background of the Midwest: a detailed mineralogical and geochemical investigation of a glacial till in southwestern Ohio. Environ Earth Sci 79:159. https://doi.org/10.1007/s12665-020-8890-z

63. Burke M, Rakovan J, Krekeler MPS (2017) A study by electron microscopy of gold and associated minerals from Round Mountain, Nevada. Ore Geol Rev 91:708–717. https://doi.org/10.1016/j.oregeorev.2017.08.026

64. Cymes B, Almquist CA, Krekeler MPS (2021) Effects of Mn(II) and Eu(III) cation exchange in sepiolite-titanium dioxide nanocomposites in the photocatalytic degradation of Orange G. ChemistrySelect 6:5180–5190. https://doi.org/10.1002/slct.202100303

65. Paul KC, Silverstein J, Krekeler MPS (2017) New insights into rare earth element particulate generated by cigarette lighters: an electron microscopy and materials science investigation of a poorly understood indoor air pollutant and constraints for urban geochemistry. Environ Earth Sci 76:369. https://doi.org/10.1007/s12665-017-6687-5

66. Post JE, McKeown DA, Heaney PJ (2020) Raman spectroscopy study of manganese oxides: tunnel structures. Am Mineral 105:1175–1190. https://doi.org/10.2138/am-2020-7390

67. Yin B, Zhang S, Jiang H, Qu F, Wu X (2015) Phase-controlled synthesis of polymorphic MnO_2 structures for electrochemical energy storage. J Mater Chem A 3(10):5722–5729. https://doi.org/10.1039/C4TA06943A

68. Hsu YK, Chen YC, Lin YG, Chen LC, Chen KH (2011) Reversible phase transformation of MnO_2 nanosheets in an electrochemical capacitor investigated by in situ Raman spectroscopy. Chem Commun 47:1252–1254. https://doi.org/10.1039/C0CC03902K

69. Patterson AL (1939) The Scherrer formula for X-ray particle size determination. Phys Rev 56:978. https://doi.org/10.1103/PhysRev.56.978

70. Makwana VD, Son YC, Howell AR, Suib SL (2002) The role of lattice oxygen in selective benzyl alcohol oxidation using OMS-2 catalyst: a kinetic and isotope-labeling study. J Catal 210:46–52. https://doi.org/10.1006/jcat.2002.3680